Injection-coupling instabilities in the BKD combustor: acoustic analysis of the isolated injectors

Philipp Brokof (CA) *, Juan Guzmán-Iñigo † and Aimee S. Morgans ‡
Department of Mechanical Engineering, Imperial College London, London, UK

Min Son§, Wolfgang Armbruster¶ and Justin S. Hardi‖
DLR, Institute of Space Propulsion, 74349 Hardthausen, Germany

Injection-coupling is a well-known cause of high frequency combustion instability in hydrogen/liquid oxygen (H2/LOX) rocket engines. This type of instability is commonly explained by the two-way coupling between the dynamics of the combustion chamber and the injection system. Recent experimental studies of the BKD combustor, however, suggest that the LOX injector could be self-excited and driving the acoustic mode of the combustion chamber. To assess the feasibility of this mechanism, here, we study both experimentally and theoretically the acoustic stability of the LOX injector isolated from the combustion chamber. The experimental study was performed in a water facility mimicking the conditions of a single LOX injector. The water injector was then modeled using an acoustic network analysis, where the transfer matrix of the LOX injector inlet orifice was computed numerically using a linear approach. The analysis successfully predicts the experimental peak in unsteady pressure, revealing that the LOX injector can be self-excited. The instability was found to be driven by the whistling of the orifice at the inlet of the injector coupled with the second longitudinal acoustic mode of the LOX post tube.

Nomenclature

A = cross section area

c = speed of sound

C_d = discharge coefficient

D = diameter

f = frequency

*Department of Mechanical Engineering, philipp.brokof@tum.de.
†Research Associate, Department of Mechanical Engineering, j.guzman-inigo@imperial.ac.uk.
‡Professor of Thermofluids, Department of Mechanical Engineering, a.morgans@imperial.ac.uk.
§Postdoc Researcher, Institute of Space Propulsion, Min.Son@dlr.de, AIAA Member
¶Topic Leader Combustion Instabilities, Institute of Space Propulsion, Wolfgang.Armbruster@dlr.de.
‖Head of Rocket Propulsion Technology Department, Institute of Space Propulsion, Justin.Hardi@dlr.de, AIAA Senior Member.

$\hat{f}$ = Riemann invariant in mean flow direction

$\hat{g}$ = Riemann invariant opposite to mean flow direction

G_0 = open loop transfer function

Γ = boundary

k = wave number

L, l = length

λ = expansion ratio

σ = complex root of acoustic network

$\dot{m}$ = mass flow rate

Ma = Mach number

ν = kinematic viscosity

ω = angular frequency

p = pressure

R = reflection coefficient

Re = Reynolds number

ρ = density

$\underline{\underline{\mathbf{S}}}$ = scattering matrix

St = Strouhal number

t = time

T = transmission coefficient

$\underline{\underline{\tau}}$ = shear stress tensor

u = velocity

x = position

Z = impedance

ζ = loss coefficient

Subscripts

d = downstream of orifice

h = orifice

n = nozzle

u = upstream of orifice

Superscripts

$\bar{\cdot}$ = time average

$\hat{\cdot}$ = Fourier transform

$\tilde{\cdot}$ = coherent perturbation

$(\cdot)'$ = turbulent fluctuation

I. Introduction

Combustion (or thermo-acoustic) instabilities pose a major risk to any new rocket engine development program. The high energy density available in the combustion chamber of rocket engines favours the excitation of such instabilities which can severely damage the engine through high amplitude pressure and temperature oscillations [1]. Discovering and remedying combustion instabilities at a late development stage is highly cost intensive. For example, more than 2000 full-scale tests were necessary to solve stability problems in the F-1 engine that was eventually used for the Apollo missions [1].

Although the phenomenon of combustion instabilities was described first by Lord Rayleigh [2] and Rijke [3] in the 19th century, it was not until the F-1 development program that it rose to attention in modern engineering applications. Since then, much work has been done to understand and predict the thermo-acoustic stability of combustion systems. Common techniques to control combustion instabilities in rocket engines [1] include adding acoustic damping by introducing resonant cavities [1], displacement of resonance frequencies by baffles [1] and the elimination of potential instability sources during early design stages. For the latter, profound knowledge of the underlying physics is necessary. While experiments give valuable insights into the physics of combustion instabilities, quantities available to measure are limited in hot-fire experiments due to the challenging conditions inside the rocket engine. Therefore, hot-fire test campaigns are usually accompanied with cold-flow experiments, numerical simulations and simplified models.

Thermo-acoustic instabilities are produced by the two-way coupling between unsteady heat release rate produced by unsteady combustion and acoustic oscillations. These instabilities can be classified as intrinsic or injection-coupled [4], depending on the physical mechanism transforming the acoustic oscillations to heat release oscillations. Intrinsic mechanisms comprise pressure-dependent chamber processes that occur after the propellants have been injected, e.g. vaporisation, that have an influence on the heat released by the combustion process. Injection-coupled mechanisms, on the other hand, rely on the oscillation of heat release due to the change of propellant flow rates in the injection system [4]. In hydrogen/liquid oxygen (H_2/LOX) engines, fuel is usually injected by shear coaxial injectors [5]. For this kind of injector, injection-coupling is a well-known cause of high frequency thermo-acoustic instability. A common explanation for this phenomenon is that the acoustics of the injector and the combustion chamber are two-way coupled [4, 6–8], in other words, mutual feedback between the combustion chamber and the injector is necessary to establish injection-coupling instabilities.

The necessity of two-way chamber/injector feedback was recently challenged by experimental results. Gröning et al.

[9] and Armbruster et al. [10] investigated combustion instabilities with the experimental research combustor model 'D' (abbr. 'BKD') operated by the German Aerospace Center (DLR), Institute of Space Propulsion in Lampoldshausen. This combustor allows unstable combustion processes under representative conditions for upper stage cryogenic rocket engines to be investigated. An instability corresponding to the first tangential mode of the combustion chamber was found in BKD and classified as injection-coupled. Furthermore, the acoustic behaviour of the LOX injector was found to be independent of the pressure fluctuations inside the combustion chamber, suggesting that the injector could be self-excited. Further studies by Armbruster et al. [10] also revealed that the self-excited behaviour was operating-condition dependent.

To explain this operating-condition, or load-point, dependency, Armbruster et al. [10] suggested that the energy driving the unsteadiness could be produced by an orifice at the inlet of the LOX injector. This orifice, used to decouple pressure oscillations in the combustion chamber from the propellant feed system, could absorb or generate acoustic energy [11, 12] (the latter called whistling). The actual acoustic behaviour of the orifice depends on a complex interplay between acoustical and vortical perturbations [13, 14] inside and in the vicinity of the orifice. For orifices with the same length-to-diameter ratio as in the BKD injector, experimental [15, 16] and numerical studies [17] show whistling at Strouhal numbers between 0.75 and 1.1, in agreement with the frequency of the experimental instability. The Strouhal number is based on the orifice length L_h, frequency f and mean bulk velocity inside the orifice U_h,

$$St = \frac{f L_h}{U_h}.$$

The experimental results suggest that the LOX injector could be self-excited by the coupling of the longitudinal modes of the injector tube with the whistling of the injector's inlet orifice. However, due to the lack of sufficient pressure oscillation data from within the injector elements of the rocket combustion chamber, this hypothesis could not be proven experimentally. To asses if the LOX injectors could be self-excited, we study them isolated from the combustor and without flames. First, experimental results obtained in a water experiment mimicking the conditions of the injector [18] are reported. This water injector is then modeled using a low-order acoustic network approach [19]. Emmert et al. [19] explain in detail the analogy between an acoustic network and a control loop in control theory. This analogy allows to apply elaborated stability analysis tools known from control theory to acoustic networks. With the Nyquist criterion [20, 21], an easily interpretable graphical approach is at hand to assess the stability of the LOX injector. However, for orifices with the length-to-diameter ratio used in the injector, reliable theoretical models are not available. Instead, the acoustic transfer function of the orifice is computed numerically using a two-step approach [22–24], where the compressible Navier-Stokes equations (LNSE) are linearized around a Reynolds-averaged mean flow. This method has achieved good results for many linear acoustic problems [22–26].

This paper is organized as follows: Section II summarizes the thermo-acoustic instability observed in hot-fire

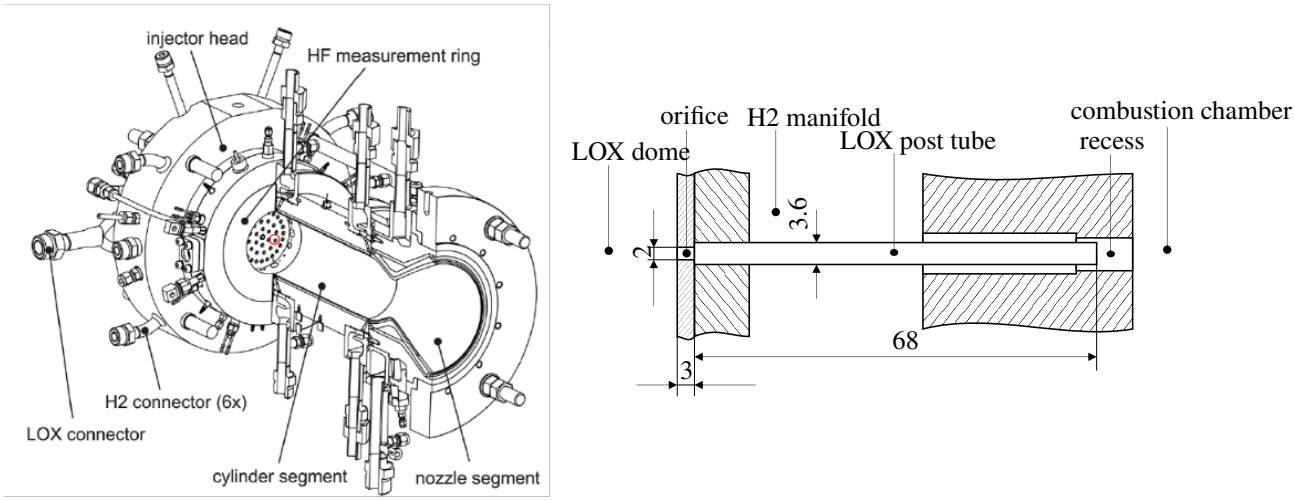

Fig. 1 Technical sketch of the experimental combustor BKD [9, 10]. Whole combustor (left) and one single injector element (right). The position of an injector in the combustor is indicated by the red circle. Dimensions are given in mm. Adapted with permission from [10]. ©2019 by Wolfgang Armbruster, Justin Hardi, Dmitry Suslov and Michael Oschwald.

experiments with the BKD combustor. Subsequently, we investigate the acoustic behaviour of the LOX injector isolated from the combustor to determine if it could be the driver of the instability. For this purpose, acoustic pressure measurements from cold-flow experiments with a single injector are presented in Section III. The stability of this experiment is analyzed using a numerical/network model approach in Section IV and, finally, an outlook on further work is given in Section V.

II. Summary of the Thermo-Acoustic Behaviour of the BKD Combustor

The research combustor BKD allows optical access to unstable combustion processes under representative conditions for upper stage LOX and hydrogen propellant rocket engines [10]. Figure 1 (left) shows a technical sketch of BKD. A measurement ring including optical access and acoustic pressure sensors is placed between the combustion chamber and the injector head. The injector head contains 42 shear coaxial injectors, through which the propellants are injected from a manifold volume, also known as dome, into the combustion chamber.

A single injector element is shown in further detail in Fig. 1 (right). Liquid oxygen flows from the LOX dome through the inlet orifice and LOX post tube to the combustion chamber. Hydrogen is injected through a concentric annulus enclosing the LOX post tube. A coaxial injector relies on shear forces between the propellant jets. To achieve high shear rates, the injection velocity of hydrogen is usually much higher than that of LOX [27]. The LOX post tube is recessed to form a mixing and pre-combustion zone. In addition, to prevent low-frequency combustion instabilities (chugging) and to ensure a homogeneous distribution of the propellant across the 42 injectors, the injector element has to decouple pressure oscillations between the combustion chamber and the propellant feed system by creating a

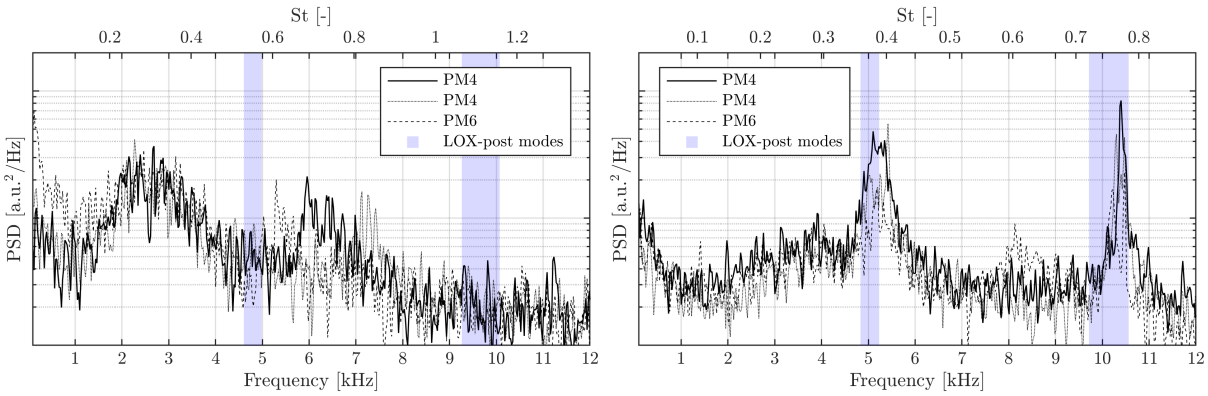

(a) LP 1 (stable) **(b) LP 2 (unstable)**

Fig. 2 Spectrum of normalized OH* emissions around the 1L and 2L modes of the LOX post tube (colored in blue).

sufficient pressure loss. For the LOX injectors, this is achieved by an orifice at the inlet of the LOX post tube [27].

For certain operating conditions, the BKD combustor exhibits a thermo-acoustic instability associated with the first tangential (1T) acoustic mode of the combustion chamber. This mode oscillates at a frequency of around 10 kHz. In previous experimental studies on the BKD combustion instability, it was found that the amplitude of the instability increases when the frequencies of the chamber 1T mode and the second longitudinal (2L) mode of the LOX injectors match, which allows the instability to be classified as injection-coupled.

To further characterize the instability, the dynamics of the flames were analyzed [9, 10] by measuring the emission of OH-radicals (OH*), which are a proxy for the unsteady heat released by the flames. Figure 2 shows the power spectral density (PSD) of OH* emissions for the stable load point LP1 and the unstable load point LP2 [10]. For the unstable load point LP2, high peaks in flame oscillations are observed around frequencies corresponding to the first (5 kHz) and second (10 kHz) longitudinal modes of the LOX post tube. The higher frequency peak at $f \approx 10$ kHz coincides with the frequency of the 1T mode (unstable for LP2 conditions). The study of Gröning et al. [9] showed that similar flame dynamics are also observed for increased chamber pressures (70 and 80 bar), where the combustor is stable because the frequencies of the chamber 1T mode and the LOX post 2L mode do not match. In contrast, for a lower chamber pressure, no peaks in flame emission can be found (Fig. 2(a) stable load point LP1) and the system remains stable despite the proximity of the frequencies of the 1T mode and the LOX post 2L mode.

The observation of the flames oscillating with the resonant frequencies of the LOX post tubes even for stable conditions, allowed Gröning et al. [9] to conclude that the oscillations are intrinsic to the injector and are not produced by feedback from the combustor. Therefore, an independent behaviour of the LOX injector causing the flame to oscillate was claimed [9, 10]. This was confirmed by Son et al. [28] who investigated the isolated LOX flow through one single injector element using Large Eddy Simulations (LES) and found self-sustained flow oscillations. These oscillations can in turn excite the chamber 1T mode if the frequency of oscillation matches the eigenfrequency of the chamber.

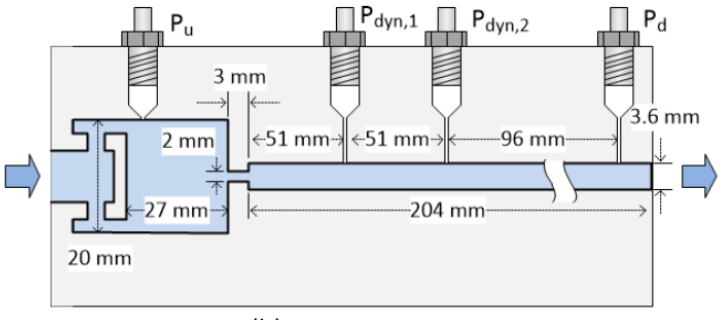

Fig. 3 Setup of the water-flow experiments with a single injector [18]. Reprinted with permission from [18]. ©2020 by Min Son, Michael Börner and Justin Hardi.

The mechanism leading to the independent self-excited behaviour of the injector is not yet clear. Armbruster et al. [10] proposed that the orifice at the inlet of the LOX post tube whistles (generates acoustic energy) and excites the first longitudinal mode of the LOX post tube (1L) at a Strouhal number of around 0.38. This mode in turn excites the overtones of the tube, including the 2L which couples with the combustion chamber. This explanation assumes that the orifice whistles at Strouhal numbers between 0.25 and 0.4 as observed for shorter holes with length-to-diameter ratios up to 0.5 [12, 15, 29–32]. However, the length-to-diameter ratio of the LOX injector inlet orifice is 1.5. In this range, the flow is expected to reattach within the hole length [33–35], in contrast with shorter holes, where the flow remains separated. This different flow topology leads to a different acoustic response, casting doubt on the assumption of whistling in the aforegiven range. In fact, a recent numerical study [17] and experimental results [15, 16] suggest a whistling range of around $0.75 \lesssim St \lesssim 1.1$ for the LOX injector orifice, opening the perspective for a direct coupling between orifice whistling and the 2L mode of the LOX post tube. This mechanism is purely linear: it does not require non-linear coupling between the fundamental and overtones of the tube. In the following, we explore the feasibility of this mechanism.

III. Experimental Study of an Isolated Injector with Water

In this section, we present non-cavitating, water flow experiments conducted with a single LOX injector [18]. The main advantage of this configuration is the better controlled acoustic boundary conditions. Since there is only one injector present, no coupling between injectors is possible as it might be the case for the hot-fire experiments. Additionally, no turbulent combustion is present at the downstream end of the tube. Figure 3 shows a schematic sketch of the experimental setup. Water enters the upstream plenum through an annular slit close to the walls and leaves the downstream tube trough a nozzle. The purpose of the nozzle is to increase the overall system pressure to avoid cavitation at the orifice. We consider an orifice with a straight inlet edge (see Son et al. [18] for a chamfered inlet edge). The non-dimensional parameters defining the geometry of the problem are the length-to-diameter ratio of the injector orifice $L_h/D_h = 1.5$, the relative length of the downstream tube $L_d/D_h = 102$ and the up- and downstream

expansion coefficients $\lambda_u = D_u/D_h = 10$, $\lambda_d = D_d/D_h = 1.8$ (see Fig. 6 for reference of the lengths and diameters). These dimensions are identical to the ones of the BKD LOX injector, but the length of the downstream tube is adapted according to the difference in speed of sound between LOX and water so that the frequencies of the modes of the post tubes are equivalent. For further information regarding the experimental setup, the reader is referred to Son et al. [18].

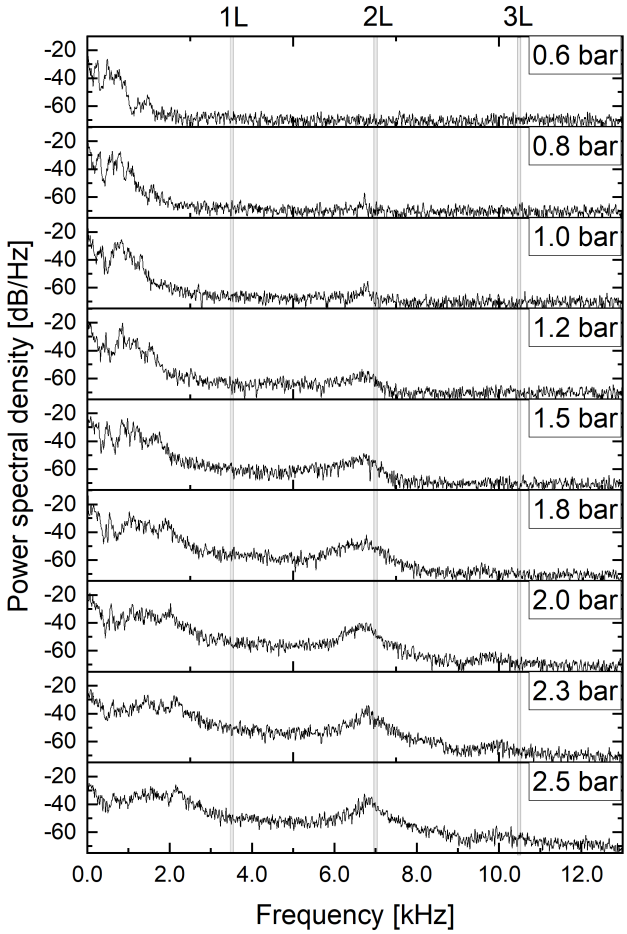

Fig. 4 PSD of dynamic pressure at sensor 1 in the downstream tube for different pressure losses across the orifice [18]. The gray lines represent the eigenfrequencies of the longitudinal modes of the downstream tube, as estimated with open-open acoustic boundary conditions. Adapted with permission from [18]. ©2020 by Min Son, Michael Börner and Justin Hardi.

Pressure oscillations were measured in the downstream duct at positions $x_1/L_d = 0.25$ and $x_2/L_d = 0.5$. Figure 4 shows the PSD of the dynamic pressure signal of the first sensor for increasing pressure drops across the orifice. For low pressure drops, the pressure signal only shows dynamics at frequencies far below the estimated 1L frequency of the downstream duct.

A strong second peak appears for pressure drops larger than 1.5 bar at a frequency coinciding with the estimated eigenfrequency of the 2L mode of the tube. For a similar orifice to that at the inlet of the injector, Brokof et al. [17] recently reported whistling in the range $0.75 \lesssim St \lesssim 1.1$. For a low pressure drop of 1.0 bar, the Strouhal number of the

2L mode is $St \approx 1.57$, which is well beyond the upper limit of the whistling range. When the pressure drop increases, the bulk velocity inside the orifice increases, which leads to a reduction of the Strouhal number of the 2L mode. When this Strouhal number moves into the frequencies of potential whistling, a peak arises. For instance, for a pressure drop of 2.5 bar, a strong oscillation is found at a Strouhal number of $St = 1.06$, suggesting that the unsteadiness could be produced by the whistling of the orifice coupled with the 2L mode of the post tube. Note that the 1L mode does not oscillate in this experiment, showing that the 2L mode can be directly excited.

For further investigation, the load points SF1 with pressure drop of 1 bar and SF2 with pressure drop of 2.5 bar are chosen and will be modeled in Sec.IV. SF1 with a comparatively small pressure peak at the 2L frequency, note that the ordinate in Fig. 4 is in logarithmic scale, is classified stable. Since the 2L frequency is an eigenfrequency of the duct, a small pressure peak is to be expected even in the stable case. SF2 with significant pressure peak at the 2L frequency is classified unstable. Each point is characterized by the Mach and Reynolds number in the orifice defined as,

$$Re_h = \frac{D_h U_h}{\nu}, \qquad Ma_h = \frac{U_h}{\bar{c}}, \tag{1}$$

respectively, where D_h is the orifice diameter, ν the kinematic viscosity and $\bar{c}$ the speed of sound inside the orifice. These non-dimensional parameters are presented in Table 1 for both load points, together with the Strouhal numbers of the observed pressure peaks. Note that while the Mach numbers in the water experiments are of the same order of magnitude as in the BKD LOX injectors, i.e. $O(10^{-2})$, the Reynolds numbers are one order of magnitude below (being $O \sim 10^6$ typical for BKD). For sufficiently high Reynolds numbers (2×10^4 [33]), the flow topology becomes independent of this parameter and, thus, the water flow will be representative of the flow in the BKD injectors.

Table 1 Load points in water experiments.

			SF1 (stable)	SF2 (unstable)
Mach number in orifice	Ma_h	[-]	8.85e-3	1.31e-2
Reynolds number in orifice	Re_h	[-]	31,000	46,100
Orifice bulk velocity	U_h	$[m/s]$	13.4	19.8
Discharge coefficient nozzle	C_d	[-]	0.8	0.76
Peak Strouhal number	St_p	[-]	-	1.0

IV. Acoustic Stability of the Water Injector

In this section, the two load points selected from the water experiment are modeled acoustically using a low-order network approach. In Sec. IV.A, the approach is introduced and results are given in Sec IV.B.

A. Low-order acoustic network of the injector

To study the acoustic stability of the water injector, acoustic models for the orifice and the downstream duct are connected in an acoustic network. The network model approach is based on the assumption that only one-dimensional acoustic waves propagate between network elements [19, 21]. The flow variables $\mathbf{Y} = (u, \rho, p)$ are split into a steady mean flow $\bar{\mathbf{Y}}$ and small-amplitude acoustic oscillations $\tilde{\mathbf{Y}}$. The acoustic perturbations are considered small compared to the mean quantities $\tilde{\mathbf{Y}} << \bar{\mathbf{Y}}$, allowing linearisation around the mean flow of the perturbation equations. The perturbation problem is formulated in the frequency domain using the ansatz $\tilde{\mathbf{Y}} = \hat{\mathbf{Y}} e^{\mathbf{i}\omega t}$.

Figure 5 shows the acoustic network model of the LOX injector (with the mean flow direction from left to right). At the inlet and outlet of the acoustic network, up- and downstream reflection coefficients R_u and R_d are defined. The amplitude and phase of the one-dimensional acoustic waves are represented by their corresponding Riemann invariants

$$\begin{aligned} \hat{f} &= \frac{1}{2}\left(\frac{\hat{p}}{\bar{\rho}\bar{c}} + \hat{u}\right), \\ \hat{g} &= \frac{1}{2}\left(\frac{\hat{p}}{\bar{\rho}\bar{c}} - \hat{u}\right), \end{aligned} \tag{2}$$

propagating in and opposite to the mean flow direction, respectively. The network is cut open between the orifice and duct by inserting a diagnostic two-port [21] to retrieve the open-loop transfer function of the network as needed for stability analysis with the Nyquist criterion. A single element in the network is characterized by its scattering matrix that links in- and outgoing waves. For example, the post tube modeled as a duct of length L without friction is described in the frequency domain by

$$\begin{pmatrix} \hat{f}_x \\ \hat{g}_x \end{pmatrix} = \underbrace{\begin{pmatrix} e^{-ik^+L} & 0 \\ 0 & e^{ik^-L} \end{pmatrix}}_{\underline{\underline{\mathbf{S}}}_{\text{duct}}} \begin{pmatrix} \hat{f}_d \\ \hat{g}_d \end{pmatrix}, \tag{3}$$

accounting for the phase difference between incident waves on the one side and outgoing waves on the other side. In the presence of a uniform mean flow of Mach number Ma, the wave numbers are defined as $k^{\pm} = \omega/[\bar{c}(1 \pm Ma)]$.

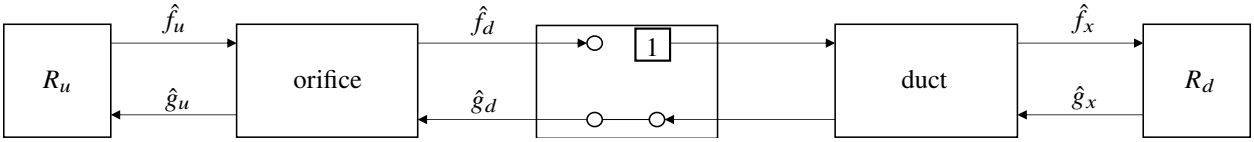

Fig. 5 Cut-open acoustic network of the LOX injector: The diagnostic two-port is inserted between the orifice and downstream duct. Mean flow direction from left to right.

In the following, we describe the modelling approach for the remaining elements of the network, namely the inlet orifice (Sec. IV.A.1) and the acoustic boundary conditions R_u and R_d (Sec. IV.A.2). Additionally, we give a brief review

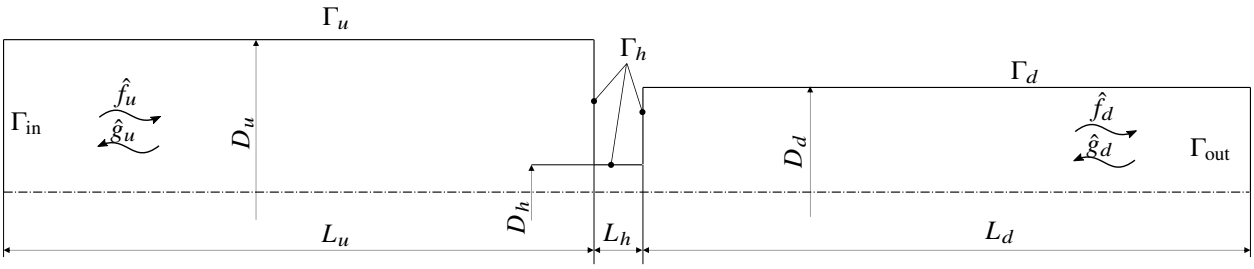

Fig. 6 Computational domain for acoustic characterisation of orifices: Rotational symmetry around the duct axis is assumed. Boundaries are denoted with $\Gamma_{(\cdot)}$. Reprinted with permission from [17]. ©2022 by Philipp Brokof, Juan Guzmán-Iñigo, Dong Yang and Aimee S. Morgans.

of the Nyquist criterion in Sec. IV.A.3.

1. Modelling of orifice acoustics

The acoustic behavior of the orifice is described by its scattering matrix which is obtained here by numerical simulations based on a two-step approach. For frequencies below the cut-off frequency of the ducts, as considered here, only plane acoustic waves are non evanescent. Therefore, to acoustically characterize the orifice, we placed it between cylindrical up- and downstream ducts that are long enough to guarantee one-dimensional wave propagation far up- and downstream of the orifice as shown in Fig. 6.

Since the Mach number in the orifice is low (see Table 1), the mean flow can be assumed incompressible and entropy fluctuations can be neglected in the perturbation field [22–24]. The flow is, therefore, completely governed by the conservation of mass and momentum,

$$\frac{\partial \rho}{\partial t} + \nabla \cdot (\rho \mathbf{u}) = 0, \tag{4}$$

$$\frac{\partial (\rho \mathbf{u})}{\partial t} + \nabla \cdot (\rho \mathbf{u} \otimes \mathbf{u}) = -\nabla p + \nabla \cdot \underline{\underline{\tau}}, \tag{5}$$

where ρ is the density, p is the pressure, $\mathbf{u}$ is the velocity. The shear stress tensor $\underline{\underline{\tau}}$ is formulated for a Newtonian fluid,

$$\underline{\underline{\tau}} = \eta \underline{\underline{\epsilon}} = \eta \left[(\nabla \mathbf{u} + \nabla \mathbf{u}^T) - \frac{2}{3} (\nabla \cdot \mathbf{u}) \underline{\underline{\mathbf{I}}} \right], \tag{6}$$

where $\underline{\underline{\epsilon}}$ is the strain rate tensor. Body forces are neglected.

We can now decompose the flow variables $\mathbf{Y} = (\mathbf{u}, \rho, p)$ into a steady mean, a coherent small-amplitude perturbation part and random turbulent fluctuations, such as $\mathbf{Y} = \bar{\mathbf{Y}} + \tilde{\mathbf{Y}} + \mathbf{Y}'$, respectively. This decomposition is introduced in Equations (4) and (5) that are, subsequently, time-averaged [36] to obtain the governing equations for the mean flow, namely the incompressible Reynolds-Averaged Navier-Stokes (RANS) equations [37]. These equations are solved with the finite volume software OpenFoam version 7.0 [38], using a segregated solver based on the SIMPLE algorithm. The

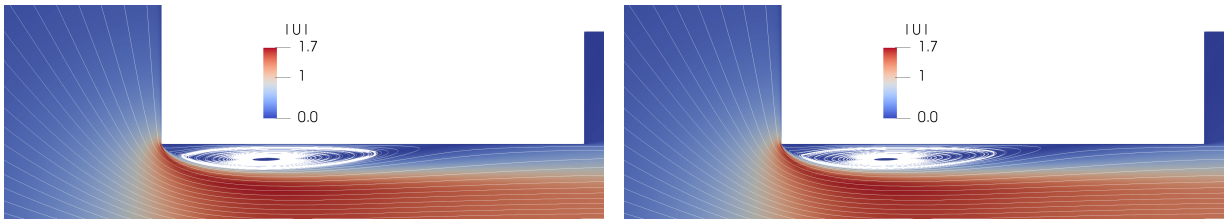

(a) SF1 **(b) SF2**

Fig. 7 Mean velocity magnitude and streamlines inside the injector orifice for load points SF1 and SF2. Velocities are normalized with orifice mean bulk velocity.

employed schemes for the fluxes are second order accurate and turbulence is modeled with the k-ω-SST turbulence model [39], which can treat wall-bounded and free-shear flows simultaneously [37, 39, 40]. This property is necessary since flow separation inside the hole and a shear layer convected downstream from the hole are present in the mean flow.

Exploiting the rotational symmetry of the problem, the structured mean flow mesh is a 5 degree wedge composed of hexahedral elements. At the duct wall upstream of the orifice Γ_u, a slip boundary condition $\bar{\mathbf{u}} \cdot \mathbf{n} = 0$ is set since it models a plenum. At the wall containing the orifice Γ_h, as well as the downstream duct wall Γ_d, no-slip boundary conditions $\bar{\mathbf{u}} = 0$ are set. At no-slip walls, the mesh resolves the boundary layer with a dimensionless wall distance of $y+ < 1$ to avoid the use of wall functions for the turbulence modelling. A uniform velocity profile with a turbulence intensity of 5% is set at the inlet Γ_{in} to yield a mean velocity of $U_h = 1$ inside the orifice. The viscosity is adjusted to match the target Reynolds number inside the orifice. Zero gradients are set for the pressure and specific dissipation rate of turbulent kinetic energy at the inlet. The flow leaves the computational domain at prescribed zero pressure and the gradients of velocity, specific dissipation rate of turbulent kinetic energy and turbulent kinetic energy are set to zero at the outlet Γ_{out}. The most important assumptions in the modeling of the orifice mean flow are rotational symmetry and the turbulence modeling.

Figure 7 shows the mean flows obtained for the stable load point SF1 and unstable load point SF2. The flow direction is from left to right. Due to the sharp inlet edge, the mean flow cannot follow the hole contour and separates. The bias flow contracts to a jet and a zone of recirculating flow establishes close to the wall. Due to the interaction of turbulent perturbations with the high mean flow shear rates inside the orifice, the flow becomes highly turbulent [41]. Re-energized by the turbulence, the flow can overcome the positive pressure gradient in the boundary layer and reattaches inside the hole. For both load cases, the mean flow reattaches at $x/L_h \approx 0.76$ measured from the inlet edge. This is in good agreement with the LES results presented in [28], where reattachment of the LOX flow through the injector was found at $x/L_h \approx 0.75$ based on the mean wall friction. This verification of the RANS solution against LES data, as well as the careful validation of the same RANS approach for a similar orifice with $L/D = 2.0$ in [17] gives confidence in the ability of the RANS approach to capture the flow topology inside the orifice for the present study.

The normalized mean flows for SF1 and SF2 are topologically very similar. This can be interpreted as follows. For

lower Reynolds numbers at which turbulence induced flow reattachment inside the orifice is not complete, the flow topology inside the orifice is strongly effected by the exact Reynolds number. In contrast, once the Reynolds number is high enough so that the flow can fully reattach within the orifice, the flow topology and especially the vena contracta does not change significantly. Experimental data by Lichtarowicz et al. [33] suggests that the discharge coefficients for orifices with $L/D = 1.0$ and $L/D = 2.0$ stabilizes at constant values for $Re > 10,000$. In the present study, the Reynolds numbers of SF1 and SF2, 31,000 and 46,100, respectively, are sufficiently high to ensure turbulent flow reattachment inside the orifice, resulting in very similar mean flow topologies.

We now turn our attention to the perturbation field. The triple decomposition is again introduced in Equations (4) and (5), the phase-average of the equations is taken and the time-average is subtracted. Neglecting second or higher order terms of the perturbation variables, the linearized Navier-Stokes equations (LNSE) are obtained as the governing equations for the perturbation dynamics, namely

$$\frac{\partial \tilde{\rho}}{\partial t} + \nabla \cdot (\bar{\rho}\tilde{\mathbf{u}} + \tilde{\rho}\bar{\mathbf{u}}) = 0, \tag{7}$$

$$\frac{\partial \bar{\rho}\tilde{\mathbf{u}}}{\partial t} + (\bar{\rho}\tilde{\mathbf{u}} + \tilde{\rho}\bar{\mathbf{u}}) \cdot \nabla\bar{\mathbf{u}} = \nabla \cdot \left(\underline{\underline{\tilde{\tau}}} - \bar{\rho}(\langle \mathbf{u}' \otimes \mathbf{u}' \rangle - \overline{\mathbf{u}' \otimes \mathbf{u}'})\right) - \nabla\tilde{p}, \tag{8}$$

where $\langle\cdot\rangle$ and $\bar{\cdot}$ denote phase and time averages, respectively. For a detailed derivation, the reader is referred to Gikadi et al. [25] and Holmberg et al. [26]. Assuming a constant speed of sound in water and neglecting entropy fluctuations, the linearized equation of state becomes $p' = \rho' \bar{c}^2$. The influence of the turbulence on the linear acoustics is modeled with a frozen eddy viscosity ν_T that is obtained from the mean flow solution, allowing closure with the Boussinesq hypothesis [25, 26]

$$\langle \mathbf{u}' \otimes \mathbf{u}' \rangle - \overline{\mathbf{u}' \otimes \mathbf{u}'} = \left[-\nu_T \left\langle \underline{\underline{\epsilon}} \right\rangle + \frac{2}{3} \langle k \rangle \underline{\underline{\mathbf{I}}}\right] + \left[\nu_T \underline{\underline{\bar{\epsilon}}} - \frac{2}{3} k \underline{\underline{\mathbf{I}}}\right] = -\nu_T \underline{\underline{\tilde{\epsilon}}}. \tag{9}$$

under the assumption that phase averaging does not affect the turbulent kinetic energy k. This approach implies that the turbulence is unaffected by the acoustic/vortical perturbations. In a last step, Eq. (7) and (8) are transformed to the frequency domain with the ansatz $\tilde{\mathbf{Y}} = \hat{\mathbf{Y}} e^{i\omega t}$.

The rotational symmetry of the problem is exploited by formulating the governing equations in cylindrical coordinates. The resulting acoustic equations are least-square stabilized and solved in the frequency domain within the finite element framework FEniCS [42] using a coupled approach [43]. Test and trial functions are polynomials of order two. An unstructured, two-dimensional mesh consisting of triangular elements is used. Anechoic acoustic boundary conditions based on a flux vector splitting approach are set at the domain inlet Γ_{in} and outlet Γ_{out} [17, 43]. Following the two-source method, the inward acoustic characteristics are separately forced at discrete frequencies once at the inlet and once at the outlet to obtain the scattering matrix of the orifice. A slip boundary condition $\hat{\mathbf{u}} \cdot \mathbf{n} = 0$ is set at the upstream duct wall

Γ_u since its purpose is to model a plenum where viscous losses are negligible. A no-slip boundary condition $\hat{\mathbf{u}} = 0$ is set at the wall containing the hole Γ_h. In the acoustic simulations, a slip boundary condition $\hat{\mathbf{u}} \cdot \mathbf{n} = 0$ is set at the downstream duct wall Γ_d to reduce the computational cost associated with the acoustic boundary layer.

The solutions of the perturbation field obtained after solving the LNSE are post-processed to extract the amplitude and phase of the one-dimensional acoustic waves traveling in and opposite to the flow direction (Riemann invariants). To this end, a numerical analogue of the multiple microphone method [44] is applied. From the Riemann invariants at the orifice inlet and outlet, the scattering matrix of the orifice and its normalized impedance are computed :

$$\begin{pmatrix} \hat{f}_d \\ \hat{g}_u \end{pmatrix}_h = \underbrace{\begin{pmatrix} T^+ & R^- \\ R^+ & T^- \end{pmatrix}}_{\underline{\underline{\mathbf{S}}}_h} \begin{pmatrix} \hat{f}_u \\ \hat{g}_d \end{pmatrix}_h, \tag{10}$$

$$Z_h = \frac{A_h}{\bar{\rho}\bar{c}} \mathcal{Z}_h = \frac{1}{\bar{\rho}\bar{c}} \frac{\Delta \hat{p}_h}{\hat{u}_h} = \frac{1}{\bar{\rho}\bar{c}} \frac{(\hat{f}_u + \hat{g}_u)_h - (\hat{f}_d + \hat{g}_d)_h}{\left(\frac{D_u}{D_h}\right)^2 (\hat{f}_u - \hat{g}_u)_h}, \tag{11}$$

where the velocity u_h is defined inside the hole at the hole inlet. The most important assumptions for the modeling of the orifice acoustics are rotational symmetry and the neglected influence of the acoustics on the turbulence. The latter assumption will stronger affect the solution at high frequencies, as perturbation length scales decrease and, hence, gradients increase.

Figure 8 shows the real Z_R and imaginary Z_I part of the impedance of the injector inlet orifice for load points SF1 and SF2. For Strouhal numbers where the resistance becomes negative, the orifice can generate acoustic energy [13, 45]. In both cases, the resistance becomes negative in the Strouhal number regime $0.85 \lesssim St \lesssim 1.15$. Additionally, a minimum with positive resistance can be found at $St \approx 0.3$.

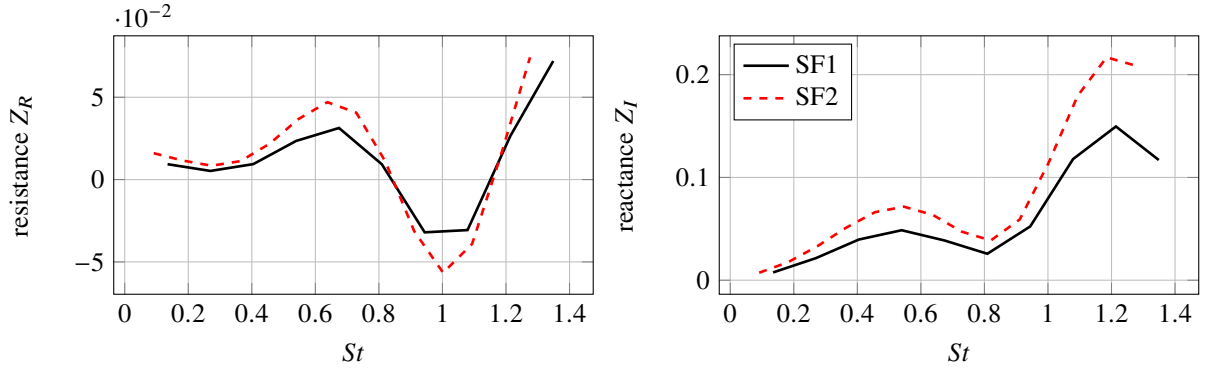

Fig. 8 Normalized impedance Z of the injector orifice for stable SF1 and unstable load points SF2.

2. Modelling of acoustic boundary conditions

The nozzle at the downstream end of the tube is modeled in the acoustic network as a compact area contraction with $A_{n,u}/A_{n,d} = 5.76$ following the model of Gentemann et al. [46]. For further information see appendix A. For the model, the acoustic loss of the area jump is estimated from the experimentally measured mean flow loss. The modelling of the downstream boundary condition is completed by assuming a plenum at the nozzle outlet, $\hat{f}_{n,d} = -\hat{g}_{n,d}$, so that the downstream reflection coefficient R_d in the acoustic network shown in Fig. 5 finally reads

$$R_d = -\frac{S_{n,11} + S_{n,21}}{S_{n,12} + S_{n,22}}. \tag{12}$$

The transfer matrix $\underline{\underline{\mathbf{S}}}_n^p$ in appendix A has been transformed into the equivalent scattering matrix $\underline{\underline{\mathbf{S}}}_n$ that links the incident and scattered acoustic waves.

Whereas the downstream duct is present in the real injector geometry, the upstream duct is introduced in the computational domain to allow wave decomposition on the upstream side of the orifice. In the real geometry, a cavity is present at the upstream side which will be modeled as a plenum with the reflection coefficient $|R_u| = 1$, $\angle R_u = 180°$, being directly imposed at the hole inlet. Therefore, the scattering matrix $\underline{\underline{\mathbf{S}}}_h^*$ is introduced which links the waves $\hat{f}_h, \hat{g}_h, \hat{f}_d, \hat{g}_d$ as shown in Fig. 9b. It is computed by scaling the Riemann invariants of the upstream duct waves $\hat{f}_u, \hat{g}_u$ to the hole inlet by assuming local incompressibility before solving for the entries of the scattering matrix. For the scaling, the velocities are related according to the incompressible continuity equation, $\hat{u}_u A_u = \hat{u}_h A_h$, and the pressures are assumed to be equal, $\hat{p}_u = \hat{p}_h$.

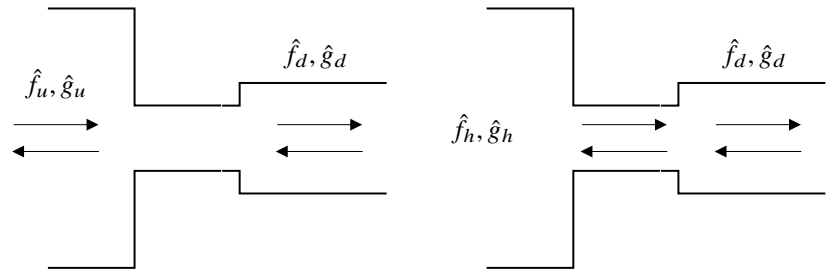

(a) Scattering matrix $\underline{\underline{\mathbf{S}}}_h$ defined between up- and downstream duct.

(b) Scattering matrix $\underline{\underline{\mathbf{S}}}_h^*$ defined between hole inlet and downstream duct.

Fig. 9 Definitions of scattering matrices across the orifice.

3. Nyquist Criterion

Across the diagnostic two-port in Fig. 5, the wave opposite to the mean flow direction $\hat{g}_d$ is propagated whereas the outgoing wave in the flow direction is set to 1. According to Polifke et al.[21], this transforms the homogeneous equation system of the closed network into an inhomogeneous equation system for the cut-open network. Both equations have the same solution if $\hat{f}_d = 1$. The open-loop transfer function is defined negative in analogy to the negative feedback

in control theory as $G_0 = -\hat{f}_d$ [47]. Hence, the mapping $\sigma \rightarrow G_0(\sigma)$ will map the roots σ of the homogeneous system into the point -1 in the complex plane. In general, these roots are complex-valued. The time domain behaviour of the system can then be obtained via the Laplace transformation as $\propto e^{i\sigma t} = e^{i\Re(\sigma)t}e^{-\Im(\sigma)t}$. Thus, unlimited exponential growth of the solution in time domain, i.e. instability, is avoided if the imaginary part of the root is positive, $\Im(\sigma) > 0$. Since $\sigma \rightarrow G_0(\sigma)$ is a conformal mapping, the Nyquist criterion for acoustic networks can be formulated as follows: The imaginary part of the eigenfrequency will be negative and the system unstable if the locus of G_0 cuts the real axis to the left of the point -1 [21].

B. Results

The open loop transfer function obtained by inserting the diagnostic two-port in the acoustic network in Fig. 5 is

$$G_0 = -\frac{R_d}{e^{i(k^+ + k^-)L}} \left(\frac{T^{*-}T^{*+}}{\frac{1}{R_u} - R^{*+}} + R^{*-} \right). \tag{13}$$

The loci obtained for the experimentally stable load point SF1 and unstable load point SF2 are shown in Fig. 10. Additionally, Fig. 11 shows the pressure PSD of both load points. In comparison to Fig. 4, here, a higher frequency resolution of the PSD calculation was chosen, in order to be able to observe more details. However, the overall trend is similar as in Fig. 4. The 1L mode is not excited in both cases and the 2L mode shows much stronger amplitudes for the case SF2. For the stable load point SF1, the locus cuts the real axis to the left of the point -1 at Strouhal numbers $St \approx 0.81$ and $St \approx 1.62$. In the pressure PSD, a small peak can be observed at $St \approx 1.5$. However, the amplitude and phase margins with which these instabilities are predicted are very small. The Strouhal numbers of the cuttings match to the signature of the system, i.e. first and second longitudinal modes of the downstream duct. At these frequencies, the system is naturally sensitive, so that small uncertainties, e.g. due to the modelling of the acoustic boundaries, will decide if the cutting is left or right of the point -1.

In contrast, the locus of the unstable load point SF2 clearly indicates an unstable root of the system for $St \approx 1.0$ which is in excellent agreement with experimental observation of a high peak in pressure fluctuations at $St \approx 1.0$ in Fig. 11. Additionally, the first eigenmode at $St \approx 0.5$ is predicted to be close to the stability border.

The results presented in this study show that the injector can generate acoustic energy in the generic environment of the water experiments, thus independent of the rest of the combustor. These findings further support the existence of a injector-driven excitation mechanism for the 1T mode of BKD as suggested by Armbruster et al. [10] and Gröning et al. [9]. The linear analysis shows that the orifice introduces acoustic energy to the system at the second eigenfrequency of the downstream duct. The fact that the orifice alone behaves very similarly for both load points shows that the instability of the injector is a result of the interplay between the orifice as the source of acoustic energy and the downstream duct as the resonator. This supports the observations of Gröning et al. [9] who were able to influence the strength of injector

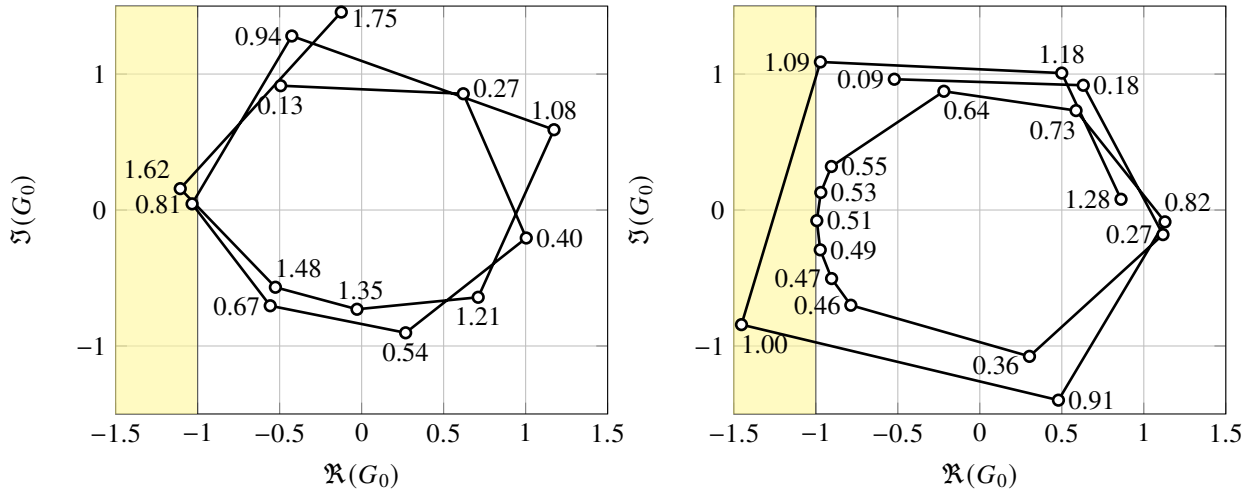

(a) SF1 **(b) SF2**

Fig. 10 Nyquist plot of the open-loop transfer function G_0 based on the two-port approach: Stable load point SF1 and unstable load point SF2.

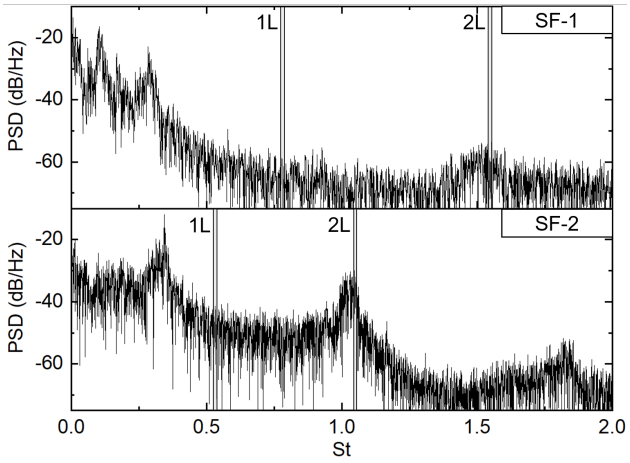

Fig. 11 Pressure PSD of stable load point SF1 and unstable load point SF2 measured in water-flow experiments.

modes in the full-scale experiments by modifying the length of the downstream ducts.

V. Conclusion and Outlook

The acoustic stability of the LOX injectors as used in the BKD experimental rocket combustor has been investigated with a linear acoustic model. To avoid uncertainties in the modelling due to turbulent combustion and injector interactions, a reference experiment comprising one single injector in a water-flow setup was studied. For low pressure drops, only one pressure peak was found at a frequency well below the eigenfrequency of the first longitudinal (1L) mode of the post tube. For a sufficiently large pressure drop, a second peak appeared in the PSD at a frequency matching the eigenfrequency of the second longitudinal (2L) mode of the post tube. The experiment shows that a direct self-excitation

of the 2L mode is possible without excitation of the 1L mode. The 2L mode is that which couples with the first tangential (1T) mode in the combustion chamber in BKD hot-fire testing to generate thermo-acoustic instability.

Two load points from the water experiment (one stable and one unstable) were selected and their acoustic stability was analyzed using a low-order network approach. The low-order network consisted of the inlet orifice and downstream duct, closed by appropriate reflection coefficients. The acoustic scattering matrix of the orifice was computed with a two-step approach. The RANS equations were solved for the mean flow and the LNSE with a frozen eddy viscosity for the perturbations. The numerical results show that for both load points, the inlet orifice has the potential to whistle in the range $0.75 \lesssim St \lesssim 1.1$. From the acoustic network analysis, the injector was found to be self-excited by whistling of its inlet orifice coupled with the 2L eigenfrequency. The instability of the water-flow experiments was captured by the analysis with an excellent agreement. Based on this analysis, the following mechanism is proposed for the 2L oscillations: When the pressure drop across the orifice increases, the mean bulk velocity in the orifice increases and this leads to a decrease of the Strouhal number of the 2L mode. When this Strouhal number reaches the upper limit of the whistling region, a self-sustained oscillation is established.

These results confirm experimental observations from hot-fire experiments [9, 10] suggesting a injector-driven instability of the chamber 1T mode caused by a hydrodynamic mechanism in the LOX injector. With the hot-fire experiments, this hypothesis could not be tested due to lacking sensor information inside the injectors. Here, we indirectly demonstrated that the LOX injector can be self-excited for certain operating conditions, with the energy provided by the whistling of the inlet's orifice. Therefore, the orifice at the LOX injector inlet should be designed with care to prevent potentially dangerous injection-driven, high-frequency combustion instabilities in the combustion chamber.

The stability analysis presented herein could in future be applied to the conditions of the hot-fire experiments. Across the injector element, the LOX density decreases by -0.18 % for LP1 and -0.35 % for LP2. This supports, in combination with the low Mach number in the orifice, the assumption of an incompressible mean flow, although the pressures are supercritical at the given temperatures. Therefore, the employed numerical two-step approach for computing the orifice scattering matrix should stay valid. However, finding reflection coefficients to terminate the acoustic network appropriately for the hot-fire experiments is challenging. The problem of defining reflection coefficients can be overcome by a coupled analysis of LOX dome and combustion chamber, where the coupling could be implemented with the injector scattering matrices obtained from the present study. Emmert et al. [48] present a universal state-space approach to connect acoustic models of different complexity that would be well suited for realising the coupling. This analysis would be able to account for tangential mode shapes in the LOX dome and combustion chamber, as well as for phase differences between the individual injectors and will be the subject of further work.

Appendix

A. Acoustic model of the nozzle as compact area jump with loss

Starting from the linearized Bernoulli and continuity equations, Gentemann et al. [46] derived the transfer matrix $\underline{\underline{\mathbf{S}}}_n^p$ for the area jump in primitive acoustic variables,

$$\begin{pmatrix} \frac{\hat{p}}{\bar{\rho}\bar{c}} \\ \hat{u} \end{pmatrix}_{n,d} = \underbrace{\begin{pmatrix} 1 & \left[1 - \zeta - \left(\frac{A_{n,u}}{A_{n,d}}\right)^2\right] Ma_{n,u} - i\frac{\omega}{\bar{c}} l_{\text{eff}} \\ -i\frac{\omega}{\bar{c}} l_{\text{red}} - Ma_{n,d} & \frac{A_{n,u}}{A_{n,d}} \end{pmatrix}}_{\underline{\underline{\mathbf{S}}}_n^p} \begin{pmatrix} \frac{\hat{p}}{\bar{\rho}\bar{c}} \\ \hat{u} \end{pmatrix}_{n,u}, \tag{14}$$

where terms of $O(Ma^2)$ and higher are neglected. The effective and reduced lengths $l_{\text{eff}}, l_{\text{red}}$ are introduced during the integration of the differential continuity and Bernoulli equation between up- $(.)_{n,u}$ and downstream $(.)_{n,d}$ side of the nozzle. Explicit expressions for the two terms are given in [46]. The loss coefficient ζ in Eq. (14) models the acoustic loss of the nozzle and is defined with respect to the downstream velocity. In the water experiments, the discharge coefficients of the nozzle were estimated to be $C_d = 0.8$ and $C_d = 0.76$ for SF1 and SF2, respectively. The discharge coefficient is defined as the ratio between the measured mass flow $\dot{m}_{\text{real}}$ and ideal loss-free mass flow $\dot{m}_{\text{ideal}}$ through the nozzle, and can be related to the mean flow pressure loss $\Delta\bar{P} = -\frac{1}{2}\bar{\zeta}\bar{\rho}\bar{u}_d^2$, where $\bar{\zeta}$ is the mean flow loss coefficient,

$$C_d = \frac{\dot{m}_{\text{real}}}{\dot{m}_{\text{ideal}}} = \sqrt{\frac{1}{1+\bar{\zeta}}}. \tag{15}$$

The combination of steady continuity and Bernoulli equation yields after linearisation the expression

$$\frac{p'_d}{\bar{\rho}\bar{c}} - \frac{p'_u}{\bar{\rho}\bar{c}} = \underbrace{\left[\left(\frac{A_u}{A_d}\right)^2 (1+\bar{\zeta}) - 1\right]}_{\zeta} Ma_u u'_u. \tag{16}$$

The constant in front of the term $Ma_u u'_u$ can be identified as an approximation for the acoustic loss ζ.

Funding Sources

The authors would like to gratefully acknowledge the support of the Erasmus+ program of the European Union and the ERC Consolidator Grant AFIRMATIVE (2018-23).

Acknowledgments

Many thanks to Dong Yang from SUSTech University for insightful discussions regarding the low-order modeling.

References

[1] Culick, F. E. C., and Yang, V., "Overview of Combustion Instabilities in Liquid-Propellant Rocket Engines," *Liquid Rocket Engine Combustion Instability*, edited by V. Young and W. E. Andersen, American Institute of Aeronautics and Astronautics, Washington, DC, 1995, Chap. 1, pp. 3–37. ISBN: 9781600864186.

[2] Rayleigh, J. W. S., *The Theory of Sound Volume 2*, 2nd ed., Dover Publications, New York, 1945. ISBN: 486602931.

[3] Rijke, P. L., "Notiz über eine neue Art, die in einer an beiden Enden offenen Röhre enthaltene Luft in Schwingung zu versetzen," *Annalen der Physik*, Vol. 183, No. 6, 1859. DOI:10.1002/andp.18591830616.

[4] Hutt, J. J., and Rocker, M., "High-Frequency Injection-Coupled Combustion Instability," *Liquid Rocket Engine Combustion Instability*, edited by V. Young and W. E. Andersen, American Institute of Aeronautics and Astronautics, Washington, DC, 1995, Chap. 12, pp. 345–355. ISBN: 9781600864186.

[5] Hulka, J., and Hutt, J. J., "Instability Phenomena in Liquid Oxygen/Hydrogen Propellant Rocket Engines," *Liquid Rocket Engine Combustion Instability*, edited by V. Young and W. E. Andersen, American Institute of Aeronautics and Astronautics, Washington, DC, 1995, Chap. 2, pp. 39–71. ISBN: 9781600864186.

[6] Kawashima, H., Kobayashi, K., Tomita, T., and Kaneko, T., "A Combustion Instability Phenomenon on a LOX/Methane Subscale Combustor," *46th AIAA/ASME/SAE/ASEE Joint Propulsion Conference & Exhibit 25 to 28 July 2010*, AIAA, Nashville, TN, 2012, pp. 2010–7082. DOI:10.2514/6.2010-7082.

[7] Scotter, J. G., Woodward, J. W., and Clayton, R., "Injector Response to Strong, High-Frequency Pressure Oscillations," *Journal of Spacecraft and Rockets*, Vol. 6, No. 4, 1969. DOI:10.2514/3.29696.

[8] Nunome, Y., Onodera, T., Sasaki, M., Tomita, T., Kobayashi, K., and Daimon, Y., "Combustion Instability Phenomena Observed During Cryogenic Hydrogen Injection Temperature Ramping Tests for Single Coaxial Injector Elements," *47th AIAA/ASME/SAE/ASEE Joint Propulsion Conference & Exhibit 31 July to 03 August 2011*, AIAA, San Diego, California, 2012, pp. 2011–6027. DOI:10.2514/6.2011-6027.

[9] Gröning, S., Hardi, J. S., Suslov, D., and Oschwald, M., "Injector-Driven Combustion Instabilites in a Hydrogen/Oxygen Rocket Combustor," *Journal of Propulsion and Power*, Vol. 32, No. 3, 2016, pp. 560–573. DOI:10.2514/1.B35768.

[10] Armbruster, W., Hardi, J. S., Suslov, D., and Oschwald, M., "Injector-Driven Flame Dynamics in a High-Pressure Multi-Element Oxygen-Hydrogen Rocket Thrust Chamber," *Journal of Propulsion and Power*, Vol. 35, No. 3, 2019, pp. 632–644. DOI:10.2514/1.B37406.

[11] Jing, X., and Sun, X., "Effect of Plate Thickness on Impedance of Perforated Plates with Bias Flow," *AIAA Journal*, Vol. 38, No. 9, 2000, pp. 1573–1578. DOI:10.2514/2.1139.

[12] Lacombe, R., Aurégan, Y., and Moussou, P., "Whistling of an Orifice in a Reverberating Duct at Low Mach Number," *The Journal of the Acoustical Society of America*, Vol. 130, 2011, pp. 2662–2667. DOI:10.1121/1.3641427.

[13] Howe, M. S., "On the Theory of Unsteady High Reynolds Number Flow Through a Circular Aperture," *Proceedings of the Royal Society London. A. Mathematical and Physical Sciences*, Vol. 366, No. 1725, 1979, pp. 205–223. DOI: 10.1098/rspa.1979.0048.

[14] Yang, D., and Morgans, A. S., "A Semi-Analytical Model for the Acoustic Impedance of Finite Length Circular Holes with Mean Flow," *Journal of Sound and Vibration*, Vol. 384, 2016, pp. 294–311. DOI:10.1016/j.jsv.2016.08.006.

[15] Moussou, P., Testud, P., Aurégan, Y., and Hirschberg, A., "An Acoustic Criterion for the Whistling of Orifices in Pipes," *ASME Pressure Vessels and Piping Conference 22 to 26 July 2007*, ASME, San Antonio, Texas, 2009, pp. 345–353. DOI:10.1115/PVP2007-26157.

[16] Testud, P., "Aéro-acoustique des diaphragmes en conduit: Sifflement et cavitation," Ph.D. thesis, Académie de Nantes, 10 2006.

[17] Brokof, P., Guzmán-Iñigo, J., Yang, D., and Morgans, A. S., "The acoustics of short circular holes with reattached bias flow," *Submitted to the Journal of Sound and Vibration*, 2022.

[18] Son, M., and Börner, M., "Experimental study of intra-injector flow fluctuations induced by a LOX injector orifice driving combustion instability," *Symposium on Thermoacoustics in Combustion: Industry meets Academia 14 to 17 September 2020*, SoTiC, Munich, Germany, 2021.

[19] Emmert, T., Jaensch, S., Sovardi, C., and Polifke, W., "taX - a Flexible Tool for Low-Order Duct Acoustic Simulation in Time and Frequency Domain," *7th Forum Acusticum 07 to 12 September 2014*, European Acoustics Association, Kraków, Poland, 2014.

[20] Leigh, J. R., *Control Theory: A guided tour*, The Institution of Engineering and Technology, 2012. ISBN: 9781849192279.

[21] Polifke, W., Paschereit, C. O., and Sattelmayer, T., "A Universally Applicable Stability Criterion for Complex Thermo-Acoustic Systems," *18. Deutsch-Niederländischer Flammentag, VDI Bericht 1313*, Delft, Netherlands, 1997, pp. 455–460.

[22] Kierkegaard, A., Boij, S., and Efraimsson, G., "A Frequency Domain Linearized Navier-Stokes Equations Approach to Acoustic Propagation in Flow Ducts with Sharp Edges," *The Journal of the Acoustical Society of America*, Vol. 2, No. 127, 2010, pp. 710–719. DOI:10.1121/1.3273899.

[23] Kierkegaard, A., Boij, S., and Efraimsson, G., "Simulations of the Scattering of Sound Waves at a Sudden Area Expansion," *Journal of Sound and Vibration*, Vol. 331, No. 5, 2012, pp. 1068–1083. DOI:10.1016/j.jsv.2011.09.011.

[24] Gikadi, J., Schulze, M., Schwing, J., Föller, S., and Sattelmayer, T., "Linearized Navier-Stokes and Euler Equations for the Determination of the Acoustic Scattering Behaviour of an Area Expansion," *18th AIAA/CEAS Aeroacoustics Conference 04 to 06 June 2012*, AIAA, Colorado Springs, 2012. DOI:10.2514/6.2012-2292.

[25] Gikadi, J., Föller, S., and Sattelmayer, T., "Impact of Turbulence on the Prediction of Linear Aeroacoustic Interactions: Acoustic Response of a Turbulent Shear Layer," *Journal of Sound and Vibration*, Vol. 333, No. 24, 2014, pp. 6548–6559. DOI:10.1016/j.jsv.2014.06.033.

[26] Holmberg, A., Kierkegaard, A., and Weng, C., "A Frequency Domain Linearized Navier-Stokes Method Including Acoustic Damping by Eddy Viscosity Using RANS," *Journal of Sound and Vibration*, Vol. 346, 2015, pp. 229–247. DOI:10.1016/j.jsv.2015.02.030.

[27] Sutton, G. P., and Biblarz, O., *Rocket Propulsion Elements*, Wiley, 2002. ISBN: 9780470080245.

[28] Son, M., Armbruster, W., Tonti, F., and Hardi, J., "Numerical Study of Acoustic Resonance In a LOX Injector post Induced by Orifice flow," *AIAA Propulsion and Energy Forum August 9 to August 11 2021*, AIAA, Virtual Event, 2021. DOI:10.2514/6.2021-3568.

[29] Testud, P., Mossou, P., Hirschberg, A., and Aurégan, Y., "Noise Generated by Cavitating Single-Hole and Multi-Hole Orifices in a Water Pipe," *Journal of Fluid and Structures*, Vol. 23, No. 2, 2007, pp. 163–189. DOI:10.1016/j.jfluidstructs.2006.08.010.

[30] Su, J., Rupp, J., Garmory, A., and Carotte, J. F., "Measurements and Computational Fluid Dynamics Predictions of the Acoustic Impedance of Orifices," *Journal of Sound and Vibration*, Vol. 352, 2015, pp. 174–191. DOI:10.1016/j.jsv.2015.05.009.

[31] Rupp, J., "Acoustic Absorption and the Unsteady Flow Associated with Circular Apertures in a Gas Turbine Environment," Ph.D. thesis, Loughborough University, 05 2013.

[32] Chen, Z., Ji, Z., and Huang, H., "Acoustic Impedance of Perforated Plates In the Presence of Bias Flow," *Journal of Sound and Vibration*, Vol. 446, 2019, pp. 159–175. DOI:10.1016/j.jsv.2019.01.031.

[33] Lichtarowicz, A., Duggins, R. K., and Markland, E., "Discharge Coefficients for Incompressible Non-Cavitating flow Through Long Orifices," *Journal of Mechanical Engineering Science*, Vol. 7, No. 2, 1965, pp. 210–219. DOI:10.1243/JMES_JOUR_1965_007_029_02.

[34] Hay, N., and Spencer, A., "Discharge Coefficients of Cooling Holes With Radiused and Chamfered Inlets," *Journal of Turbomachinery*, Vol. 114, No. 4, 1992, pp. 701–706. DOI:10.1115/1.2928022.

[35] Idelchik, I. E., *Handbook of Hydraulic Resistance*, 4th ed., Begell House, 2007. ISBN: 9781567002515.

[36] Hussain, A. K. M. F., and Reynolds, W. C., "The Mechanics of Organized Wave in Turbulent Shear Flow," *Journal of Fluid Mechanics*, Vol. 41, No. 2, 1970, pp. 241–258. DOI:10.1017/S0022112070000605.

[37] Wilcox, D. C., *Turbulence Modeling for CFD*, 3rd ed., DCW Industries, La Caąda, Calif, 2006. ISBN: 1928729088.

[38] Weller, H. G., Tabor, G., Jasak, H., and Fureby, C., "A Tensorial Approach to Computational Continuum Mechanics Using Object-Orientated Techniques," *Computers in Physics*, Vol. 12, 1998, pp. 620–631. DOI:10.1063/1.168744.

[39] Menter, F. R., Knutz, M., and Langtry, R., "Ten Years of Industrial Experience with the SST Turbulence Model," *4th International Symposium Turbulence, heat and mass transfer 2003*, Begell House, Inc., Antalya, Turkey, 2003. ISBN: 1567001963.

[40] Guzmán-Iñigo, J., Yang, D., Johnson, H. G., and Morgans, A. S., "Sensitivity of the Acoustics of Short Circular Holes with Bias Flow to Inlet Edge Geometries," *AIAA Journal*, Vol. 57, No. 11, 2019, pp. 4835–4844. DOI:10.2514/1.J057996.

[41] Pope, S., *Turbulent Flows*, Cambridge University Press, Cambridge, 2000. ISBN: 9780521598866.

[42] Alnæs, M., Blechta, J., Hake, J., Johansson, A., Kehlet, B., Logg, A., Richardson, C., Ring, J., Rognes, M. E., and Wells, G. N., "The FEniCS Project Version 1.5," *Archive of Numerical Software*, Vol. 3, No. 100, 2015, pp. 9–23. DOI:10.11588/ans.2015.100.20553.

[43] Guzmán-Iñigo, J., Yang, D., Gaudron, R., and Morgans, A. S., "On the scattering of entropy waves at sudden area expansions," *Submitted to the Journal of Sound and Vibration*, 2021.

[44] Jang, S.-H., and Ih, J.-G., "On the Multiple Microphone Method for Measuring In-Duct Acoustic Properties in the Presence of Mean Flow," *The Journal of the Acoustical Society of America*, Vol. 103, No. 3, 1998. DOI:10.1121/1.421289.

[45] Fabre, D., Longobardi, R., Bonnefis, P., and Luchini, P., "The Acoustic Impedance of a Laminar Viscous Jet Though a Thin Circular Aperture," *Journal of Fluid Mechanics*, Vol. 864, 2019, pp. 5–44. DOI:10.1017/jfm.2018.1008.

[46] Gentemann, A. M. G., Fischer, A., Evesque, S., and Polifke, W., "Acoustic Transfer Matrix Reconstruction and Analysis for Ducts with Sudden Change of Area," *9th AIAA/CEAS Aeroacoustics Conference and Exhibit 12 to 14 May 2003*, AIAA/CEAS, South Carolina, 2012, pp. 1–11. DOI:10.2514/6.2003-3142.

[47] Kopitz, J., and Polifke, W., "CFD-Based Application of the Nyquist Criterion to Thermo-Acoustic Instabilities," *Journal of Computational Physics*, Vol. 227, No. 14, 2008, pp. 6754–6778. DOI:10.1016/j.jcp.2008.03.022.

[48] Emmert, T., Meindl, M., Jaensch, S., and Polifke, W., "Linear State Space Interconnect Modelling of Acoustic Systems," *Acta Acustica united with Acustica*, Vol. 102, No. 5, 2016, pp. 824–833. DOI:10.3813/AAA.918997.